Electrochemical Sensor for Biofilm Based on the Detection of NADH by Polythiophene Nanoparticles

Brenda G. Molina,[1,2] Luis J. del Valle,[1,2] Pau Turon,[3] Elaine Armelin,[1,2,*] and Carlos Alemán[1,2,4,*]

[1] *Departament d'Enginyeria Química, EEBE, Universitat Politècnica de Catalunya, C/ Eduard Maristany, 10-14, Ed. I2, 08019, Barcelona, Spain*

[2] *Barcelona Research Center for Multiscale Science and Engineering, Universitat Politècnica de Catalunya, C/ Eduard Maristany, 10-14, Ed. C, 08019, Barcelona, Spain*

[3] *B. Braun Surgical, S.A. Carretera de Terrasa 121, 08191 Rubí (Barcelona), Spain*

[4] *Institute for Bioengineering of Catalonia (IBEC), The Barcelona Institute of Science and Technology, Baldiri Reixac 10-12, 08028 Barcelona Spain*

Correspondence to: elaine.armelin@upc.edu and carlos.aleman@upc.edu

ABSTRACT

Composite i-PP/PEDOT films made of isotactic polypropylene (i-PP), which is frequently used for the fabrication of implantable medical devices for internal use, and chemically synthesized poly(3,4-ethylendioxythiophene) (PEDOT) nanoparticles, which are electroactive and biocompatible, have been prepared and used to detect biofilm infection. After chemical and morphological characterization, the properties (interfacial, mechanical, thermal and electrochemical) and biocompatibility of i-PP/PEDOT have been examined. Besides, carbon screen-printed electrodes coated with i-PP/PEDOT have been found to detect the growth of Gram-positive and Gram-negative bacteria through the oxidation of nicotinamide adenine dinucleotide (NADH), which comes from the bacteria metabolism (*i.e.* the respiration). Thus, as outer bacterial membranes are permeable to cytosolic NADH, this metabolite has been found to be an appropriated target for the detection of growing bacterial infections (biofilms). In addition, the sensor does not respond towards eukaryotic cells. This is because the major NADH pool in eukaryotic cells is located at the mitochondria and, therefore, the concentration of in the medium is not high enough to be detected since the inner mitochondrial membrane is impermeable to NADH or NAD+.

INTRODUCTION

Bacteria embed themselves in a hydrated extracellular matrix of polysaccharides and proteins, forming a slimy layer known as a biofilm. Biofilms, which are considered as an adaptation of microbes to hostile environments,[1] are generated after initial adhesion of bacteria onto any kind of living or inert surface and their subsequent immobilization growth and reproduction. During the growth phase, bacteria produce extracellular biopolymers that extend developing a complex matrix of molecular fibers with unique characteristics. Although some exceptions have been reported,[2] the most important one is, in general, its capacity to hinder the access of antimicrobials through it.[2-4] As a consequence, adhered microorganisms increase their antimicrobial resistance, becoming up to one thousand times more resistant to antibiotics.

In the biomedical field, bacterial biofilm infections, which are typically associated with patients with indwelling devices for the purpose of medical treatments,[5] attract significant clinical investigations since one established, biofilm becomes difficult to be eradicated. Thus, with the progress of medical sciences, the application of medical prostheses and implantable devices in the treatment of human diseases is experiencing an exponential growing and, therefore, bacterial biofilm infections become also frequent. Unfortunately, the vast majority of internal (*e.g.* vascular prosthesis,[6] cerebrospinal fluid shunts,[7] prosthetic heart valves[8] and breast implants[9]) and external (e.g. dentures[10] and contact lenses[11]) prostheses, as well as hip prosthesis (*i.e.* when hip joints are replaced by prosthetic implants) may result in biofilm colonization of the devices. New strategies for preventing and detecting in early stage biofilm related infections become therefore challenging and attract significant attention.

One of the emerging methods for biofilm detection is the use of electrochemical impedance spectroscopy (EIS) measures by employing polymeric sensors.[12-17] In EIS,

the electrochemical impedance across the electrode-electrolyte interface is measured over a wide range of frequencies to elicit information about the properties of the interface. In the case of biofilms, successful detection is based on changes linked to charge transfer resistance and capacitance corresponding to the maturing stages of biofilm development. However, analysis of the electrical behaviour of biofilm development is not an easy challenge and development of simplified methodologies is highly desirable to make affordable such objective.

In this work cyclic voltammetry (CV) has been used to detect the presence of bacteria while eukaryotic cells remain undetected. As CV is typically employed to identify the redox state of biomolecules, as for example neurotransmitters (*e.g.* dopamine[18,19] and serotonine[20]), glucose,[21,22] and opioids,[23,24] we have focused our attention in nicotinamide adenine dinucleotide (NADH). This biomolecule plays an important role not only as cofactor for numerous deshydrogenase enzymes but also in the electron transfer chain in living organisms.[25-27] Thus, NADH and its oxidized form (NAD+) mediates many redox reactions, providing the major source of ATP for aerobic organisms.[26,27] In addition to energy metabolism of living cells, NADH/NAD+ are closely associated with many pathological states, such as aging, diabetes, cancer and neurological diseases.[28-31]

Eukaryotic cells present two major NADH pools, the cytosolic and the mitochondrial pools.[32] Although aerobic respiration reactions in eukaryotic cells take place in mitochondria, the mitochondrial and cytosolic NADH ratio is cell-type specific.[33] However, a distinctive characteristic is that mitochondrial double-membrane is impermeable to NADH or NAD+ (*i.e.* the outer membrane is quite permeable but the inner membrane is highly folded into cristae), mitochondrial NADH levels being maintained even upon massive depletion of cytosolic NADH.[31,34] In opposition, as

prokaryotes do not have mitochondria, their respiration occurs in the cytosol or on the inner surfaces of the cell membrane. Therefore, as prokaryote cellular membranes are permeable to NADH and NAD+ and a gradient is expected, the extracellular detection of these species could be an appropriated target for monitoring growing bacterial infections or biofilms.

Here we address two questions: (1) Is it possible to distinguish the bacterial growth, and the consequent formation of biofilm, from the growth of eukaryotic cells through the voltammetric detection of NADH (*i.e.* the oxidation from NADH to NAD+)?; and (2) could such voltammetric sensor be manufactured using biocompatible materials and integrated into smart biomedical prostheses for monitoring bacterial quantification and biofilm colonization?. To address these questions, composites made of isotactic polypropylene (i-PP) and poly(3,4-ethylendioxythiophene) nanoparticles (PEDOT NPs), hereafter denoted i-PP/PEDOT, have been developed. i-PP is used for the fabrication of internal prostheses, as for example surgical meshes for hernia repair while PEDOT NPs, which are biocompatible,[35,36] are expected to reduce the overpotential for NADH oxidation, to accelerate the electron transfer between NADH and the electrode, and to minimize the presence of competing reactions.

METHODS

The materials and the characterization methods, which involved dynamic light scattering (DLS), scanning electron microscopy (SEM), FTIR and micro-Raman spectroscopies, wettability, stress-strain, calorimetric, thermogravimetric and electrochemical measures, are provided in the Electronic Supporting Information (ESI).

Synthesis of PEDOT NPs. PEDOT NPs were prepared adapting a previously reported procedure.[37] In brief, an aqueous micellar solution was prepared by stirring

(750 rpm) a solution of 0.07 g of 4-dodecylbenzenesulfonic acid (DBSA) in 20 mL of milli-Q water for 1 hour. This was followed by the addition of 11.8 mg of 3,4-ethylenedioxythiophene (EDOT) monomer and, again, was stirred (750 rpm) for 1 hour at room temperature. Finally, 0.45 g of ammonium persulfate (APS) dissolved in 5 mL of milli-Q water was added to the solution. Then, the reaction was maintained in agitation at 30 ºC for 24 hours protected from light with aluminium foil. In this process, the colour of the reaction mixture changed from light grey to dark blue.

No sedimentation was observed after the reaction, indicating a good colloidal stability. The resultant solution was centrifuged (11000 rpm) for 40 min at 4 °C. The supernatant solution was decanted and the sediment was re-dispersed in milli-Q water using an ultrasonic bath for 15 min at 30 °C. The centrifugation and re-dispersion process was conducted two more times to ensure the elimination of side products and unreacted chemicals, purifying the dispersion medium. Finally, the last pellet was kept under vacuum two days and, subsequently, was weighted and re-dispersed in the corresponding media at the desired concentration.

Preparation of i-PP films. In order to dissolve polymer pellets, 3 g of i-PP (M_n = 50000 g/mol, M_w = 190000 g/mol, and polydispersity index= 3.80) and 100 mL of xylene were loaded in a round bottom flask equipped with a magnetic stirrer. The solution was heated on an oil bath set at 130 ºC and continuously stirred (250 rpm) until the pellets were completely dissolved. Then, the temperature was decreased to 120 ºC, maintained at such conditions for 20 min, and cooled to room temperature. After that, the polymer was precipitated by adding 400 mL of methanol. The polymer was separated by filtration, washed with methanol for three times, and put in a ventilation hood during 48 hour for solvent evaporation. The recovered product was dried at 50 ºC for 24 hours.

i-PP films were prepared in a hydraulic press of 15 tons equipment with Atlas series heated platens. For this purpose, 0.1 g of polymer powder were placed in the press, heated until 180 ºC and, after 5 min, the pressure was increased from 0 to 5 tons. After 2.5 min, the pressure was increased to 7 tons and maintained for 2.5 min more. Finally, the film was removed from the press and cooled to room temperature.

Preparation of porous i-PP films. i-PP powder was composited with 10% w/w NaCl by mechanical stirring at 1000 rpm for 12 hours. Films were obtained by pressing the powder mixture following the procedure previously explained. Porous films were obtained by dissolving the NaCl particles with deionized water. Films were kept immersed for periods of 12 hours until the weight of the dry sample was stable (*i.e.* water was changed every period). Hereafter, the porous films resulting from such process have been denoted i-PP(p) to differentiate them from compact i-PP films.

Preparation of i-PP/PEDOT films. i-PP/PEDOT films were prepared by incorporating PEDOT NPs to the initial mixture, as described for i-PP(p). PEDOT NPs were added considering 40 or 60 % w/w with respect to the i-PP weight. The films resulting from such concentrations were denoted i-PP/PEDOT(40%) and i-PP/PEDOT(60%), respectively.

Adhesion and proliferation of bacteria. *Escherichia coli* (*E. coli*) and *Staphylococcus aureus* (*S. aureus*), which are Gram-negative and Gram-positive bacteria, respectively, were selected to evaluate the adhesion and initial growth (24 hours) and proliferation (7 days) of prokaryotic cells in contact with the i-PP and i-PP/PEDOT samples. The bacteria were previously grown aerobically to exponential phase in broth culture (5 g/L beef extract, 5 g/L NaCl, 10 g/L tryptone, pH 7.2).

2×10^8 colony forming units (CFU) per mL were seeded in 10 mL of culture DMEM high glucose supplemented with 2% FBS (pH 8.1) and 0.2% $NaHCO_3$. Bacterial growth

curves in that supplemented medium are displayed in Figure S1. After 24 hours, 150 µL were added to 5 mL of $NaHCO_3$ supplemented DMEM in sterile vials containing i-PP, i-PP(p), i-PP/PEDOT(40%) and i-PP/PEDOT(60%) films. Controls were simultaneously performed by culturing cells in sterile vials without material. All samples, including the control, were vortexed for 1 min and incubated at 37 ºC with agitation at 80 rpm for 24 hours and 7 days for cell growth. UV absorbance was measured at λ= 450 nm in a flat-bottomed 96 well-plates with aliquots of 200 µL. The results, derived from the average of three replicates (*n*=3) for each independent experiment, were normalized with the control for relative percentages.

Adhesion and proliferation of eukaryotic cells. Cellular assays were performed using Cos-1 and Vero cells. These cells were selected due to their fast growth. Cells were cultured in DMEM high glucose buffered with 2.5 mM of HEPES, 10% FBS, penicillin (100 units/mL), and streptomycin (100 µg/mL). The cultures were maintained in a humidified incubator with an atmosphere of 5% CO_2 and 95% O_2 at 37 ºC. Culture media were changed every two days. When the cells reached 80-90% confluence, they were detached using 2 mL of trypsin (0.25% trypsin/EDTA) for 2-5 min at 37 °C. Finally, cells were re-suspended in 5 mL of fresh medium and their concentration was determined by counting with a Neubauer camera using 0.4% trypan blue as a vital dye.

i-PP and i-PP/PEDOT films were placed in plates of 24 wells and sterilized using UV irradiation for 15 min in a laminar flux cabinet. Controls were simultaneously performed by culturing cells on the surface of TCPS plates. For adhesion and proliferation assays 2×10^4 and 1×10^4 Cos-1 and Vero cells, respectively, were deposited on the film of each well. Then, attachment of cells to the film surface was promoted by incubating under culture conditions for 30 min. Finally, 2 mL of the culture medium were added to each well. After 24 h, cellular adhesion was determined by quantifying

the cells attached to the films or the control. Cellular proliferation was evaluated by quantifying the viable cells onto the evaluated materials after 7 days of culture.

Cellular viability was evaluated by the colorimetric MTT [3-(4,5-dimethylthiazol-2-yl)-2,5-diphenyltetrazolium bromide] assay, which is described in the ESI.

Electrochemical detection of prokaryotic vs. eukaryotic cells. The electrochemical detection of prokaryotic *vs.* eukaryotic cells was performed by CV using the Autolab PGSTAT302N. Experiments were conducted in the cell culture media at room temperature. The initial and final potentials were −0.20 V while the reversal potential was +0.60 V. A scan rate of 100 mV s^{-1} was applied in all cases. An Ag|AgCl 3 M KCl and a Pt-wire were used as reference electrode and counter electrode, respectively. The working electrode consisted on a carbon screen-printed electrode (SPE) from Dropsens (DRP-150) coated with a gelatin layer, which was used to adhere the i-PP and i-PP/PEDOT films. Such adhesive layer was prepared by dissolving 50 mg of gelatin from porcine skin in 1 mL of milli-Q water, which was placed in an ultrasonic bath at 40 °C for 15 minutes until a clear solution was acquired. A solution drop (10 μL) was deposited onto the SPE surface and, subsequently, a round film of i-PP or i-PP/PEDOT (4 mm in diameter) was placed onto the resulting gelatin-modified SPE. All experiments were replicated three times.

RESULTS AND DISCUSSION

Preparation and characterization

Figure 1a displays a micrograph of the prepared PEDOT NPs, which present a coral-like morphology and exhibit an effective diameter of 48±9 and 91±1 nm as determined by SEM and DLS, respectively. The FTIR spectra of EDOT monomer and PEDOT NPs doped with DBSA are compared in Figure S2. The monomer shows bands at 3109 and

772 cm^{-1} which correspond to the C^{α}–H stretching and out-of-plane vibration modes, respectively. The disappearance of these two absorption bands in the polymer spectrum proves the success of the polymerization process, reflecting that the hydrogen atoms at the C^{α}-position were removed during the formation of PEDOT NPs. Among the bands the bands identified in the polymer spectrum, which are discussed in the ESI, the peak at 1719 cm^{-1} deserves consideration. It corresponds to the carbonyl group formed by the irreversible overoxidation of the thiophene ring and indicates that PEDOT NPs are overoxidized. Interestingly, overoxidized PEDOT was reported to exhibit unique sensitivity for the detection of biomolecules, such as dopamine and uric acid.[38,39] On the other hand, the FTIR spectra of i-PP, i-PP(p), i-PP/PEDOT(40%) and i-PP/PEDOT(60%) films, which display an average thickness of 47±5, 74±5, 81±4 and 76±4 μm, respectively, are completely dominated by the polyolefin absorption bands (Figure S3).

The bands identified in the Raman spectrum of i-PP (Figure 1b) are: 809 (CH_2 rocking and C–C stretching), 843 (CH_2 rocking) 973 (CH_3 rocking and C–C stretching), 998 (CH_3 rocking), 1151 (C–C stretching, C–H bending), 1120 (CH_2 twisting, CH wagging and C–C stretching), and 1436 cm^{-1} (CH_2 deformation).[40-42] Moreover, the CH_3 vibrations at 973 cm^{-1} are attributed to the 3_1 helical conformation of crystalline i-PP chains, while the CH_3 rocking at 998 cm^{-1} involves segments with such helical structure.[41] The normalized integral intensity of the bands at 809 and 843 cm^{-1} was proposed to be an estimation of the crystallinity (χ_c) of i-PP.[40] The former band is related with chains in regular helical conformations, while the latter is associated with conformational defects and chains with non-helical conformations. The χ_c value derived from the 809 and 843 cm^{-1} bands is 51% and 40%, respectively, the average value (46%) being fully consistent with that derived from melting thermograms (see below).

Figure 1b includes the Raman spectra of PEDOT NPs, i-PP/PEDOT(40%) and i-PP/PEDOT(60%). The Raman fingerprints of PEDOT were reported in previous studies:[43-45] 1424 cm^{-1} (symmetric $C_\alpha=C_\beta$ stretching), 1490 cm^{-1} (asymmetric $C_\alpha=C_\beta$ stretching), 1368 cm^{-1} ($C_\alpha–C_{\alpha'}$ inter-ring stretching), 708 cm^{-1} (symmetric C–S–C deformation), 856 cm^{-1} (asymmetric C–S–C deformation) and 991 cm^{-1} (O–C–C–O ring deformation). The bands of PEDOT NPs are clearly identified in the Raman spectra of i-PP/PEDOT films, which look very different from the spectrum of the neat i-PP. The complementary information provided by the FTIR and Raman spectra confirms the integration of PEDOT NPs into the polyolefin matrix of i-PP/PEDOT films. Besides, camera photographs displayed in Figure 1c shows that the whitish color of neat i-PP films turns into very dark blue when the PEDOT NPs are incorporated.

Figure 2a displays photographs and SEM micrographs of the different films prepared in this work. i-PP exhibits an homogeneous and compact surface morphology, whereas a distribution of closed and non-interconnected micropores are clearly distinguished on the surface of i-PP(p) films. Thus, the concentration of NaCl is too low to create contact between particles, precluding the formation of networks of interconnected pores crossing the entire film thickness. i-PP/PEDOT micrographs present light spots distributed on the surface, which correspond to micro-aggregates of PEDOT NPs, as was proved by the signal of sulfur in the energy dispersive X-ray (EDX) spectra (Figure S4). As it was expected, both size and amount of spots, which are responsible for the change of color of i-PP film, increase with the concentration of PEDOT NPs. More specifically, the average diameter of the micro-aggregates is 4.0±1.1 and 5.1±2.4 μm for i-PP/PEDOT(40%) and i-PP/PEDOT(60%), respectively.

Wettability affects the cellular response of materials.[46] The water contact angle (WCA) of PEDOT films was reported to be ~80º,[47] reflecting a poor hydrophilic

behaviour. Comparison of the WCA values measured for the different films prepared in this work (Figure S5), indicate that PEDOT NPs do not cause significant changes in the hydrophobic response of i-PP (*i.e.* WCA > 90º in all cases). The alteration of the surface topography by forming non-interconnected pores and by introducing PEDOT NPs only reduced the WCA of neat i-PP (108º±1º) by 9-13º.

On the other hand, the incorporation of pores and, especially, PEDOT NPs was in detriment of the mechanical properties of i-PP (Figure S6). The addition of PEDOT drastically reduced the Young modulus (~50%), the tensile strength (~70%) and the elongation at break (~50%) due to the aggregation of the NPs. Thus, aggregates behaved as fracture sites participating in the initiation and/or propagation of the mechanical failure. These effects are more pronounced with the increasing NPs concentration since the interfacial adhesion between the i-PP matrix and the PEDOT aggregates become weaker, facilitating the detachment of the latter from the matrix. Also, the incorporation of PEDOT NPs drastically reduces the ductility of i-PP matrix, which undergoes a stiffening effect that drastically decreases the elongation at break.

Calorimetric data were obtained by differential scanning calorimetry (DSC) and thermogravimetric analyses (TGA). DSC melting and crystallization curves of neat i-PP and i-PP/PEDOT composites are shown in Figures 2b-c, while the characteristics from those runs are summarized in Table S1. Neat i-PP displays two melting peak temperatures at T_{m1}= 155 ºC and T_{m2}= 162 ºC, which correspond to the melting of β- and α-type crystals, respectively. Incorporation of PEDOT NPs results in small shifts of the T_m values (*e.g.* T_{m1}= 158 ºC and T_{m2}= 164 ºC for i-PP/PEDOT(40%)), which have been attributed to small increments of the crystal sizes, and in an enhancement of the heat flow at the T_{m2} peak, which illustrates that PEDOT NPs favour the formation of α-type i-PP. Besides, when cooled at 10 ºC/min, the crystallization temperature of neat i-

PP (T_c= 122 ºC) increases 3-4 ºC upon the incorporation of PEDOT NPs, suggesting that the latter act as nucleating agents. However, the χ_c values calculated from the melting thermograms (Eqn 1 in the ESI) indicate that size of the crystals decreases upon the incorporation of PEDOT NPs (*i.e.* χ_c= 33-36% for i-PP/PEDOT and χ_c= 44% for neat i-PP). This could be attributed to the poor interfacial adhesion between i-PP crystals and PEDOT NPs. On the other hand, TGA curves (Figure S7) show that the CP NPs affect the thermal stability and the decomposition mechanism of the i-PP matrix. Details are discussed in the ESI.

Control voltammograms for bare and film-modified electrodes in 0.1 M PBS (pH 7.4), are displayed in Figure 3a. The lack of anodic and cathodic peaks in the voltammograms recorded for i-PP(p) indicates that oxidation and reduction processes do not occur at specific positions of polymer chains. However, the shape of the voltammogram changes with increasing number of oxidation-reduction cycles (Figure 3b), becoming similar to that of the bare electrode. Moreover, the voltammetric charge (|Q|) increases from 7±3 μC (first control voltammogram) to 19±2 μC after 500 redox cycles (Figure 3e), reflecting an increment of electroactivity (Figure 3f). Both the variation in the shape and the increment of electroactivity suggest that i-PP(p) films undergo chemical or structural degradation during the electrochemically induced redox processes (see below).

On the other hand, the control voltammograms of the two i-PP/PEDOT composites (Figures 3a, 3c and 3d) resemble those reported for neat PEDOT films,[47,48] with an anodic peak at approximately –0.1 V and a cathodic peak at a potential slightly lower than the reversal potential. As observed for i-PP(p), |Q| increases with the number of consecutive redox cycles for both i-PP/PEDOT(40%) and i-PP/PEDOT(60%) (Figure 3e). This infrequent "*self-electrostabilizing*" effect is much more pronounced for latter

composite than for the former one. Thus, after 500 consecutive redox cycles Q| increases from 17±3 to 32±2 μC and from 13±3 to 56±4 μC for i-PP/PEDOT(40%) and i-PP/PEDOT(60%) (Figure 3e), respectively, which represents an increment in the electroactivity of ~190% and ~330% (Figure 3f), respectively.

The FTIR spectra recorded before and after 500 consecutive redox cycles are very similar for i-PP(p) and i-PP/PEDOT (Figure S8), indicating that i-PP does not undergo significant chemical changes. Therefore, the self-electrostabilizing effect observed in Figures 3 cannot be attributed to the chemical degradation of the i-PP matrix. In contrast, SEM images of i-PP(p) and i-PP/PEDOT after 500 redox cycles, which are displayed in Figure S9, indicate important structural changes in the films. After 500 cycles, microfractures appeared on the surface of i-PP(p) films (Figure S9a) due to the stress induced by the potential scans. In the case of i-PP/PEDOT(40%) and i-PP/PEDOT(60%) (Figures S9b-c), the structural stress is adsorbed by some PEDOT aggregates that end up detaching. The shape and size of the resulting pores are defined by the characteristics of detached PEDOT particles, which are very varied. The increment of the surface porosity facilitates the access and escape of ions during the oxidation and reduction processes, respectively, explaining the unusually observed self-electrostabilizing behaviour.

Adhesion and proliferation of prokaryotic and eukaryotic cells

The adhesion and initial growing (24 hours) and long-term proliferation (7 days) of prokaryotic and eukaryotic cells onto i-PP, i-PP(p), i-PP/PEDOT were evaluated considering different bacteria and eukaryotic cell lines. Regarding to prokaryotic cells, *E. coli* and *S. aureus*, which are Gram-negative and Gram-positive bacteria, respectively, were incubated onto such films. The extent of the antimicrobial activity

(*i.e.* bacterial growth) was quantified by analyzing the turbidity of the incubated bacteria cultures after 24 hours and 7 days by UV-vis spectroscopy at λ= 450 nm. The relative viabilities after 24 hours (Figure 4a, left) are very similar to that of the TCPS control, indicating that bacteria do not exhibit a specific attraction towards i-PP, i-PP(p) and i-PP/PEDOT. However, long-term bacterial growth was observed after 7 days, especially onto i-PP/PEDOT films (Figure 4a, right), relative to the control. Specifically, PEDOT-containing samples benefits the growth of both Gram-positive and Gram-negative bacteria. This undesirable effect could be mitigated by introducing gold nanoparticles (Au-NPs) into the PEDOT matrix either during or after the polymerization process. Thus, plasmonic Au-NPs, that efficiently convert near-infrared light into heat, have been found to inhibit bacterial growth around them,[49] thus preventing any undesirable effect in the detection process.

The ability of i-PP, i-PP(p), i-PP/PEDOT(40%) and i-PP/PEDOT(60%) films to enhance the adhesion and proliferation of eukaryotic cells are compared in Figure 4b. As it can be seen, the cellular adhesion onto the composite films is conditioned by the i-PP matrix, which presents the lowest relative viability for Vero and, especially, Cos-1 cells. Specifically, after 24 h, Cos-1 viability is ~40% lower for i-PP and i-PP/(p) than for the control, while the incorporation of CP results in an increment of the viability that depends on the NPs concentration. The number of cells on the surface of all films increases after 7 days. Results confirm that cell adhesion onto the composite films is easier than onto the i-PP ones, this tendency increasing with the concentration of PEDOT NPs. Although the viabilities obtained for the Vero cell line are higher for all prepared films than for the control, Cos-1 cells clearly prefer the composite films than the i-PP and i-PP(p) films. This behavior has been attributed to the ion exchange ability

of the electroactive CP, which favours the exchange of electrolytes with cell at the interface defined by the surface of the film and the cell membrane.

On the detection of bacterial cells while fingerprints of eukaryotic cells remain undetected

In this section, the performance of the i-PP/PEDOT composite for the *in situ* electrochemical detection of biofilm contamination is examined through the oxidation of NADH to NAD+. With the aim of orienting this sensor towards clinical applications, the fingerprints of eukaryotic and prokaryotic cells colonizing a medical device should be differentiated. Therefore, we focused on monitoring the metabolism of prokaryotic and eukaryotic cells using carbon SPEs coated with i-PP/PEDOT(40%) since the load of PEDOT NPs is smaller and display properties similar to i-PP/PEDOT(60%). The growth of bacteria and eukaryotic cells was following by examining the electrochemical response of the medium at different times, which range from 0 (just when the cells are introduced in the culture medium) to 24 hours.

Figure 5a displays the response of the sensor to the culture medium without cells at different incubation times. As it can be seen, cyclic voltammograms are similar to those displayed in Figure 3, independently of the incubation time, indicating that the response coming from the oxidization of species contained in the $NaHCO_3$ supplemented DMEM is practically null. Accordingly, the anodic current at the reversal potential ($j_{0.6}$), 0.60 V, only decreases from 13 to 11 $\mu A/cm^2$ after 24 hours. In opposition, i-PP/PEDOT(40%) is remarkably affected by the presence of cultured bacteria, even though the response of the sensor against *E. coli* and *S. aureus* are different and change with the incubation time (Figures 5b-c). Thus, an oxidation peak at 0.60 V is clearly observed in both cases. This has been attributed to the oxidation of NADH to NAD+. Previous studies on

PEDOT-based electrodes reported that the oxidation peak of NADH in a solution without the presence of bacteria can be found between 0.5 V (i.e. processable PEDOT colloidal microparticles)[50] and 0.70 V (i.e.electrochemically synthesized graphene-PEDOT:PSS).[51] Thus, the detection of the of NADH to NAD+ is indicative of bacterial activity.[52,53] Moreover, the current density at 0.60 V varies with the incubation time (Figure 5d), reflecting that i-PP/PEDOT(40%) detects that the bacteria growth is very fast at the first stages of incubation. For *E. coli*, $j_{0.6}$ increases from 8 to 171 μA/cm^2 after 2 hours, decreasing to 161 μA/cm^2 after 24 hours. For *S. aureus*, the $j_{0.6}$ value is 298 μA/cm^2 after 24 hours of culture, which is consistent with the cell viability measurements displayed in Figure 4a (*i.e.* adhesion was higher for the Gram-positive bacterium than for the Gram-negative one). However, analysis of the temporal evolution of $j_{0.6}$ displayed in Figure 5d allows monitoring that in the first stages the growing of *E. coli* is faster than of *S. aureus*. It should be remarked that no change of color associated to the pH indicator contained in the DMEM supplement was detected in the culture medium during the bacteria growth. Accordingly, the pH was preserved during the whole detection process and, therefore, the surface of the sensor remained unaffected by acidic metabolism of the bacteria.

Analysis of Figure 5d shows that $j_{0.6}$ reaches a plateau before biofilm formation, which is expected to occur after ~24 h. This feature is especially striking for *E. coli* since the plateau is reached very fast. In a first assumption this observation could be attributed to the saturation of PEDOT NPs in the electrode and/or to limitations in the linear dynamic range. More specifically, the adsorption of oxidized analytes onto the electroactive materials used as electrodes and their subsequent saturation is a well-known limitation of some electrochemical biosensors. Besides, the huge amount of bacteria involved in biofilms requires that a very high interval of CFU/mL over which

the sensor response is linear. The plateaus reached in Figure 5d could be interpreted as the loss of the linear regime, which eventually could limit the quantitative utilization of the sensor. However, comparison of the profiles displayed in Figure 5d with Figure 5e, which shows to the growth of *E. coli* and *S. aureus* in the culture medium against the incubation time as determined UV-vis spectroscopy, suggest that the limitations discussed above are less decisive than expected. Thus, the variation of the absorbance at 450 nm with the incubation time agrees with the profiles electrochemically obtained for the two bacteria (Figure 5d), evidencing the capacity of the sensor for detecting the presence of growing bacteria. The calibration curve (Figure 5f), which was approximated using the McFarland standard, indicates that the amount of *E. coli* and *S. aureus* bacteria grow from 1.6×10^8 CFU/mL (first measure for both types) to 1.7×10^8 and 2.4×10^8 CFU/mL, respectively, after 24 h. These results are fully consistent with the electrochemical sensing measures displayed in Figures 5b-c.

The selectivity with respect eukaryotic cells is crucial for the performance and practical application of the sensor in medical devices. Figure 6 proves that the electrochemical response of i-PP/PEDOT(40%) against the growth of eukaryotic cells is completely different to that displayed for bacteria. Cyclic voltammograms recorded just after the addition of Cos-1 and Vero cells are practically identical to those obtained after 24 hours of cell culture (not shown) and very similar to those achieved after 7 days of cell proliferation (Figure 6). Moreover, after such long time $j_{0.6}$ only increases from 7 to 10 $\mu A/cm^2$ and from 9 to 11 $\mu A/cm^2$ for Cos-1 and Vero cells, respectively, evidencing that the concentration of NADH induced by such eukaryotic cells is not high enough to be detected by the i-PP/PEDOT sensor.

Results displayed in Figures 5 and 6 clearly indicate that the i-PP/PEDOT(40%) sensor distinguishes bacteria while eukaryotic cells remain undetected. This behavior

originates from the sensitivity of the i-PP/PEDOT composite towards the oxidation of NADH, which is high enough to detect the metabolism of bacteria but too low for the respiration of eukaryotic cells. In addition, the oxidation of NADH towards NAD+ probably causes an electrochemically-induced concentration gradient, favouring the exit of cytosolic NADH to the medium through the outer bacterial membrane and, consequently, facilitating the detection of the bacterial metabolism.

CONCLUSIONS

In this study, simple and highly sensitive biosensors have successfully developed for the detection of bacteria growth through the oxidation of NADH. In a first stage the sensors, which are based on PEDOT NPs supported into an i-PP matrix, have been characterized by FTIR and Raman spectroscopies, SEM, contact angle measurements, mechanical tests, differential scanning calorimetry and thermogravimetry analyses. Although the mechanical and thermal properties of i-PP/PEDOT composites are affected by the interfacial adhesion between their components, the combination of i-PP and PEDOT NPs is very attractive in terms of electrochemical properties. Thus, the electrochemical processes observed for i-PP/PEDOT are similar to those described for neat PEDOT films and, in addition, the composite exhibits self-electrostabilizing behaviour. This unusual characteristic, which consists in the increase of electrochemical activity as the number of consecutive redox cycles grow, is due to an increment in the surface porosity of the films.

The i-PP/PEDOT sensor detects the growth of Gram-negative and Gram-positive bacteria through the oxidation of the NADH, which comes from bacterial metabolism and permeates through the outer membrane to the extracellular culture medium. In contrast, the NADH produced by the respiration of eukaryotic cells remains in the

mitochondria pool and, therefore, the presence of those cells e not interfering with the readings of the bacterial sensor. The prepared sensor, which can be produced at low cost, is deemed to be of high clinical interest as it might be the first line of defence against biofilm formation benefit in a number of scenarios where bacteria colonize the implanted medical devices competing with healthy eukaryotic cells.

ACKNOWLEDGEMENTS

Authors acknowledge MINECO/FEDER (MAT2015-69367-R and RTI2018-098951-B-I00), the Agència de Gestió d'Ajuts Universitaris i de Recerca (2017SGR359) and B. Braun Surgical, S.A. company for financial support. Support for the research of C.A. was received through the prize “ICREA Academia” for excellence in research funded by the Generalitat de Catalunya. B. G. M. is thankful to CONACYT for the financial support through a postgraduate scholarship (328467 CVU 621314).

SUPPORTING INFORMATION

The Supporting Information is available free of charge on the ACS Publications website at DOI:XXXXX. Description of the Methods, FTIR spectra, mechanical and thermal properties, and SEM micrographs of the sensors after a high number of oxidation and reduction cycles.

REFERENCES

1. Hall-Stoodley, L.; Costerton, J. W.; Stoodley, P. Bacterial Biofilms: from the Natural Environment to Infectious Diseases. *Nat. Rev. Microbiol.* **2004**, *2*, 95–108.
2. Fux, C. A.; Costerton, J. W.; Stewart, P. S.; Stoodley, P. Survival Strategies of Infectious Biofilms. *Trends Microbiol.* **2005**, *13*, 34–40.

3. Lebeaux, D.; Chauhan, A.; Rendueles, O.; Beloin, C. From *in Vitro* to *in Vivo* Models of Bacterial Biofilm-Related Infections. *Pathogens* **2013**, *2*, 288–356.
4. Hoiby, N.; Bjarnsholt, T.; Givskov, M.; Molin, S.; Ciofu, O. Antibiotic Resistance of Bacterial Biofilms. *Int. J. Antimicrob. Agents* **2010**, *35*, 322–332.
5. Hetrick, E. M.; Schoenfisch, M. H. Reducing Implant-Related Infections: Active Release Strategies. *Chem. Soc. Rev.* **2006**, *35*, 780–789.
6. Tollefson, D. F.; Bandyk, D. F.; Kaebnick, H. W.; Seabrook, G. R.; Towne, J. B. Surface Biofilm Disruption. Enhanced Recovery of Microorganisms from Vascular Prostheses. *Arch. Surg.* **1987**, *122*, 38–43.
7. Fux, C. A.; Quigley, M.; Worel, A. M.; Post, C.; Zimmerli, S.; Ehrjich, G.; Veeh, R. H. Biofilm-Related Infections of Cerebrospinal Fluid Shunts. *Clin. Microbiol. Infect.* **2006**, *12*, 331–337.
8. Donlan, R. M. Biofilms and Device-Associated Infections. *Emerg. Infect. Dis.* **2001**, *7*, 277–281.
9. Rieger, U. M.; Mesina, J.; Kalbermatten, D. F.; Haug, M.; Frey, H. P.; Pico, R.; Frei, R.; Pierer, G.; Lüscher, N. J.; Trampuz, A. Bacterial Biofilms and Capsular Contracture in Patients with Breast Implants. *Br. J. Surg.* **2013**, *100*, 768–774.
10. Murakami, M.; Nishi, Y.; Seto, K.; Yamashita, Y.; Nagaoka, E. Dry Mouth and Denture Plaque Microflora in Complete Denture and Palatal Obturator Prosthesis Wearers. *Gerodontology* **2015**, *32*, 188–194.
11. Abidi, S. H.; Sherwani, S. K.; Siddiqui, T. R.; Bashir, A.; Kazmir, S. U. Drug Resistance Profile and Biofilm Forming Potential of *Pseudomonas Aeruginosa* Isolated from Contact Lenses in Karachi-Pakistan. *BMC Ophthalmol*. **2013**, *13*, 57.

12. Dheilly, A.; Linossier, I.; Darchen, A.; Hadjiev, D.; Corbel, C.; Alonso, V. Monitoring of Microbial Adhesion and Biofilm Growth Using Electrochemical Impedancemetry. *Appl. Microbiol. Biotechnol.* **2008**, *79*, 157–164.
13. Ben-Yoav, H.; Freeman, A.; Sternheim, M.; Shacham-Diamand, Y. An Electrochemical Impedance Model for Integrated Bacterial Biofilms. *Electrochim. Acta* **2011**, *56*, 7780–7786.
14. Zheng, L. Y.; Congdon, R. B.; Sadik, O. A.; Marques, C. N. H.; Davies, D. G.; Sammakia, B. G.; Lesperance, L. M.; Turner, J. N. *Sens. Actuators B* **2013**, *182*, 725– 732.
15. Ward, A. C.; Hannah, A. J.; Kendrick, S. L.; Tucker, N. P.; MacGregor, G.; Connolly, P. Identification and Characterisation of *Staphylococcus Aureus* on Low Cost Screen Printed Carbon Electrodes Using Impedance Spectroscopy. *Biosens. Bioelectron.* 2018, **110**, 65–70.
16. van Duuren, J. B. J. H.; Müsken, M.; Karge, B.; Tomasch, J.; Wittmann, C.; Häussler, S.; Brönstrup, M. Use of Single-Frequency Impedance Spectroscopy to Characterize the Growth Dynamics of Biofilm Formation in Pseudomonas aeruginosa. *Sci. Rep.* **2017**, *7*, 5223.
17. Paredes, J.; Becerro, S.; Arana, S. Label-Free Interdigitated Microelectrode Based Biosensors for Bacterial Biofilm Growth Monitoring Using Petri Dishes. *J. Microbiol. Methods* **2014**, *100*, 77–83.
18. Fabregat, G.; Córdova-Mateo, E.; Armelin, E.; Bertran, O.; Alemán, C. Ultrathin Films of Polypyrrole Derivatives for Dopamine Detection. *J. Phys. Chem. C* **2011**, *115*, 14933–11941.

19. Fabregat, G.; Armelin, E.; Alemán, C. Selective Detection of Dopamine Combining Multilayers of Conducting Polymers with Gold Nanoparticles. *J. Phys. Chem. B* **2014**, *118*, 4669–4682.
20. Molina, B. G.; Cianga, L.; Bendrea, A.-D.; Cianga, I.; del Valle, L. J.; Estrany, F.; Alemán, C.; Armelin, E. Amphiphilic Polypyrrole-Poly(Schiff base) Copolymers with Poly(ethylene glycol) Side Chains: Synthesis, Properties and Applications. *Polym. Chem.* **2018**, *9*, 4218–4232.
21. Buendía, J. J.; Fabregat, G.; Castedo, A.; Llorca, J.; Alemán, C. Plasma-Treated Polyethylene as Electrochemical Mediator for Enzymatic Glucose Sensors: Toward Bifunctional Glucose and Dopamine Sensors. *Plasma Proc. Polym.* **2018**, *15*, e1700133.
22. Hocevar, M. A.; Fabregat, G.; Armelin, E.; Ferreira, C. A.; Alemán, C. Nanometric Polythiophene Films with Electrocatalytic Activity for Non-Enzymatic Detection of Glucose. *Eur. Polym. J.* **2016**, *79*, 132–139.
23. Teixeira-Dias, B.; Alemán, C.; Estrany, F.; Azambuja, D. S.; Armelin, E. Microstructures of Poly(N-methylpyrrole) and Their Interaction with Morphine. *Electrochim. Acta* **2011**, *56*, 5836–5843.
24. Córdova-Mateo, E.; Poater, J.; Teixeira-Dias, B.; Bertran, O.; Estrany, F.; del Valle, L. J.; Sola, M.; Alemán, C. Electroactive Polymers for the Detection of Morphine. *J. Polym. Res.* **2014**, *21*, 565.
25. Ricci, F.; Amine, A.; Moscone, D.; Palleschi, G. A Probe for NADH and H_2O_2 Amperometric Detection at Low Applied Potential for Oxidase and Dehydrogenase Based Biosensor Applications. *Biosens.Bioelectron.* **2007**, *22*, 854–862.
26. R. C. Bohinski, Oxidative Phosphorylation. In Modern Concepts in Biochemistry, Newton, MA: Bacon, Inc., 1987, pp. 567–604.

27. Wos, M. L.; Pollard, P. C. Cellular Nicotinamide Adenine Dinucleotide (NADH) As an Indicator of Bacterial Metabolic Activity Dynamics in Activated Sludge. *Water. Sci Technol.* **2009**, *60*, 783–791.

28. Lin, S. J.; Guarente, L. Nicotinamide Adenine Dinucleotide, a Metabolic Regulator of Transcription, Longevity and Disease. *Curr. Opin. Cell Biol.* **2003**, *15*, 241–246.

29. Zhang, Q.; Wang, S. Y.; Nottke, A. C.; Rocheleau, J. V.; Piston, D. W.; Goodman, R. H. Redox Sensor CtBP Mediates Hypoxia-Induced Tumor Cell Migration. *Proc. Natl. Acad. Sci. USA* **2006**, *103*, 9029–9033.

30. Garriga-Canut, M.; Schoenike, B.; Qazi, R.; Bergendah, K.; Daley, T. J.; Pfender, R. M.; Morrison, J. F; Ockuly, J.; Satstrom, C.; Sutula, T.; et al. 2-Deoxy-D-Glucose Reduces Epilepsy Progression by NRSF-CtBP-Dependent Metabolic Regulation of Chromatin Structure. *Nat. Neurosci.* **2006**, *9*, 1382–1387.

31. Ying, W. NAD+ and NADH in Brain Functions, Brain Diseases and Brain Aging. *Front. Biosci.* **2007**, *12*, 1863–1888.

32. Ying, W. NAD+/NADH and NADP+/NADPH in Cellular Functions and Cell Death: Regulation and Biological Consequences. *Antioxid. Redox Signal.* **2008**, *10*, 179–206.

33. Stein, L. R.; Imai, S.-i. The Dynamic Regulation of NAD Metabolism in Mitochondria. *Trends Endocrinol. Metab.* **2012**, *23*, 420–428.

34. Pittelli, M.; Formentini, L.; Faraco, G.; Lapucci, A.; Rapizzi, E.; Cialdai, F.; Romano, G.; Moneti, G.; Moroni, F.; Chiarugi, A. Inhibition of Nicotinamide Phosphoribosyltransferase: Cellular Bioenergetics Reveals a Mitochondrial Insensitive NAD Pool. *J. Biol. Chem.* **2010**, *285*, 34106–34114.

35. Del Valle, L. J.; Aradilla, D.; Oliver, R.; Sepulcre, F.; Gamez, A.; Armelin, E.; Alemán, C.; Estrany, F. Cellular Adhesion and Proliferation on Poly(3,4-

ethylenedioxythiophene): Benefits in the Electroactivity of the Conducting Polymer. *Eur. Polym. J.* **2007**, *43*, 2342–2349.

36. Del Valle, L. J.; Estrany, F.; Armelin, E.; Oliver, R.; Alemán, C. Cellular Adhesion, Proliferation and Viability on Conducting Polymer Substrates. *Macromol. Biosci.* **2008**, *8*, 1144–1151.
37. Puiggalí-Jou, A.; Micheletti, P.; Estrany, F.; del Valle, L. J.; Alemán, C. Electrostimulated Release of Neutral Drugs from Polythiophene Nanoparticles: Smart Regulation of Drug-Polymer Interactions. *Adv. Health. Mater.* **2017**, *6*, 1700453.
38. Lin, J. M.; Su, Y. L.; Chang, W. T.; Su, W., Y.; Cheng, S. H. Strong Adsorption Characteristics of a Novel Overoxidized Poly(3,4-ethylenedioxythiophene) Film and Application for Dopamine Sensing. *Electrochim. Acta* **2014**, *149*, 65–75.
39. Özcan, A.; Ilkbaş, S. Preparation of Poly(3,4-ethylenedioxythiophene) Nanofibers Modified Pencil Graphite Electrode and Investigation of Over-Oxidation Conditions for the Selective and Sensitive Determination of Uric Acid in Body Fluids. *Anal. Chim. Acta* **2015**, *891*, 312–320.
40. Nielsen, A. S.; Batchelder, D. N.; Pyrz, R. Estimation of Crystallinity of Isotactic Polypropylene Using Raman Spectroscopy. *Polymer* **2002**, *43*, 2671–2676.
41. Zerbi, G.; Gussoni, M.; Ciampelli, F. Structure of Liquid Isotactic Polypropylene from Its Vibrational Spectrum. *Spectrochim. Acta* **1967**, *23A*, 301–311.
42. Tadokoro, H.; Kobayashi, M.; Ukita, M.; Yasufuku, K.; Mtirahashi, S.; Torii, T.Normal Vibrations of the Polymer Molecules of Helical Conformation. V. Isotactic Polypropylene and Its Deuteroderivatives. *J. Chem. Phys.* **1965**, *42*, 1432–1449.

43. Garreau, S.; Duvail, J. L.; Louarn, G. Spectroelectrochemical Studies of Poly(3,4-Ethylenedioxythiophene) in Aqueous Medium. *Synth. Met.* **2002**, *125*, 325–329.
44. Han, Y.-K.; Chang, M.-Y.; Huang, W.-Y.; Pan, H.-Y.; Ho, K.-S.; Hsieh T.-H.; Pan, S.-Y. Improved Performance of Polymer Solar Cells Featuring One-Dimensional PEDOT Nanorods in a Modified Buffer Layer. *J. Electrochem. Soc.* **2011**, *158*, K88–K93.
45. Farah, A. A.; Rutledge, S. A.; Schaarschmidt, A.; Lai, R.; Freedman, J. P.; Helmy, A. S. Conductivity Enhancement of Poly(3,4ethylenedioxythiophene)-Poly(styrenesulfonate) Films Post-Spincasting. *J. Appl. Phys.* **2012**, ***112***, 113709.
46. Pérez-Madrigal, M. M.; Giannotti, M. I.; del Valle, L. J.; Franco, L.; Armelin, E.; Puiggalí, J.; Sanz, F.; Alemán, C. Thermoplastic Polyurethane:Polythiophene Nanomembranes for Biomedical and Biotechnological Applications. *ACS Appl. Mater. Interfaces* **2014**, *6*, 9719–9732.
47. Maione, S.; Gil, A. M.; Fabregat, G.; del Valle, L. J.; Triguero, J.; Laurent, A.; Jacquemin, D.; Estrany, F.; Jiménez, A. I.; Zanuy, D.; et al. Electroactive Polymer–Peptide Conjugates for Adhesive Biointerfaces. *Biomater. Sci.* **2015**, *3*, 1395–1405.
48. Fabregat, G.; Ballano, G.; Armelin, E.; del Valle, L. J.; Cativiela, C.; Alemán, C. An Electroactive and Biologically Responsive Hybrid Conjugate Based on Chemical Similarity. *Polym. Chem.* **2013**, *4*, 1412–1424.
49. de Miguel, I.; Prieto, I.; Albornoz, A.; Sanz, V.; Weis, C.; Turon, P.; Quidant, R. Plasmon-Based Biofilm Inhibition on Surgical Implants. *Nano Lett.* **2019**, *19*, 2524–2529.
50. Meng, L.; Turner, A. P. F.; Mak, W. C. Positively-Charged Hierarchical PEDOT Interface with Enhanced Electrode Kinetics for NADH-Based Biosensors. *Biosens. Bioelectron.* **2018**, *120*, 115–121.

51. Sriprachuabwong, C.; Karuwan, C.; Wisitsorrat, A.; Phokharatkul, D.; Lomas, T.; Sritongkham, P.; Tuantranon, A. Inkjet-Printed Graphene-PEDOT:PSS Modified Screen Printed Carbon Electrode for Biochemical Sensing. *J. Mater. Chem.* **2012**, *22*, 5478–5485

52. Hung, Y. P.; Albeck, J. G.; Tantama, M.; Yellen, G. Imaging Cytosolic NADH-NAD(+) Redox State with a Genetically Encoded Fluorescent Biosensor. *Cell Metabolism* **2011**, *14*, 545–554.

53. Vinogradov, A. D.; Grivennikova, V. G. Oxidation of NADH and ROS Production by Respiratory Complex I. *Biochim. Biophys. Acta, Bioenerg.* **2016**, *1857*, 863–871.

CAPTIONS TO FIGURES

Figure 1. (a) SEM micrograph of PEDOT NPs (left) and effective diameter histogram derived from SEM measurements (right). (b) Raman spectra (left) and optical micrographs recorded with the Raman microscope (right) of PEDOT NPs and i-PP, i-PP/PEDOT(40%) and i-PP/PEDOT(60%) films. (c) Photographs of i-PP, i-PP(p), i-PP/PEDOT(40%) and i-PP/PEDOT(60%) films

Figure 2. (a) SEM micrographs of i-PP, i-PP(p), i-PP/PEDOT(40%) and i-PP/PEDOT(60%) films. The light spots observed in i-PP/PEDOT films correspond to micro-aggregates of PEDOT NPs, as was evidenced by EDX spectroscopy (Figure S4). For neat i-PP and both i-PP/PEDOT(40%) and i-PP/PEDOT(60%) composites: selected regions of the DSC thermograms portraying the (a) melting and the (b) crystallization.

Figure 3. (a) Control voltammograms of bare and modified SPEs. The latter were obtained by assembling i-PP(p), i-PP/PEDOT(40%) or i-PP/PEDOT(60%) films onto the surface of the SPEs using gelatin as intermediate layer. Cyclic voltammograms recorded after a variable number of consecutive oxidation-reduction cycles: (b) i-PP(p), (c) i-PP/PEDOT(40%) and (d) i-PP/PEDOT(60%). Variation of (e) the measured voltammetric charge (|Q|) and (f) the loss of electrochemical activity (LEA) against the number of consecutive redox cycles for i-PP(p), i-PP/PEDOT(40%) and i-PP/PEDOT(60%).

Figure 4. Cellular adhesion (left) and cellular proliferation (right) on i-PP, i-PP(p), i-PP/PEDOT(40%), i-PP/PEDOT(60%) films. Assays were performed using (a) two representative bacteria (*E. coli* and *S. aureus*) and (b) two representative eukaryotic cells (Cos-1 and Vero). Three samples were analyzed for each group. Bars represent the mean standard deviation. The relative viability was established in relation to the control

(100%). The asterisk (*) indicates a significant difference with the control, Tukey's test (p<0.03).

Figure 5. Cyclic voltammograms for i-PP/PEDOT(40%) in the culture medium ($NaHCO_3$ supplemented DMEM) recorded at different incubation times: (a) in absence of bacteria; (b) in presence of *E. coli*; and (c) in presence of *S. aureus*. Initial and final potentials: -0.20 V; reversal potential: 0.60 V; and scan rate: 100 mV/s. (d) Variation of the current density at 0.60 V ($j_{0.6}$) with the incubation time for (a), (b) and (c). (e) Variation of the absorbance at 450 nm with the incubation time as determined in the culture medium ($NaHCO_3$ supplemented DMEM) in absence of bacteria and in presence of *E. coli* and *S. aureus*. (f) Calibration curve obtained using the McFarland standard to approximate the number of bacteria as a function of the absorbance.

Figure 6. Cyclic voltammograms for i-PP/PEDOT(40%) in the culture medium recorded just after the addition of the cells and after seven days of incubation: (a) in absence of cells; (b) in presence of Cos-1 cells; and (c) in presence of Vero cells.

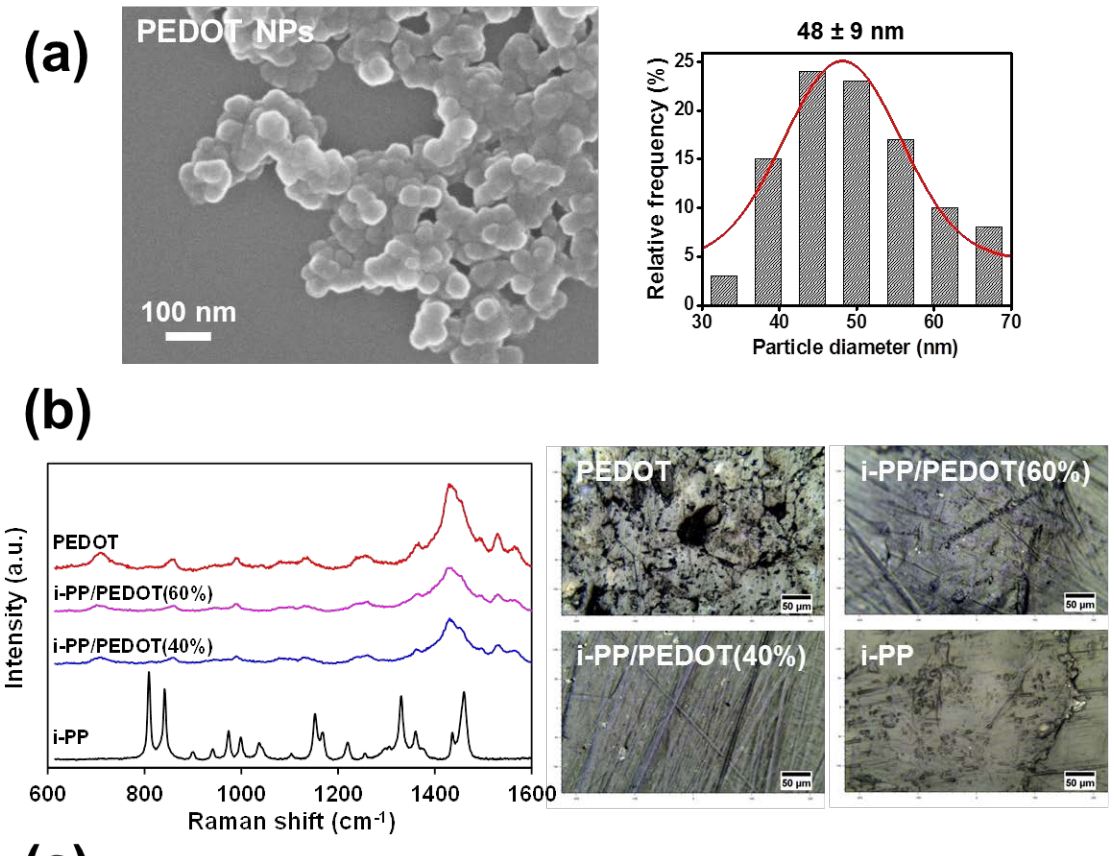
(a)
PEDOT NPs
100 nm
48 ± 9 nm
Relative frequency (%)
Particle diameter (nm)
(b)
Intensity (a.u.)
PEDOT
i-PP/PEDOT(60%)
i-PP/PEDOT(40%)
i-PP
Raman shift (cm-1)
PEDOT
i-PP/PEDOT(60%)
i-PP/PEDOT(40%)
i-PP
(c)
i-PP
i-PP(p)
i-PP/PEDOT(40%)
i-PP/PEDOT(60%)

Figure 1

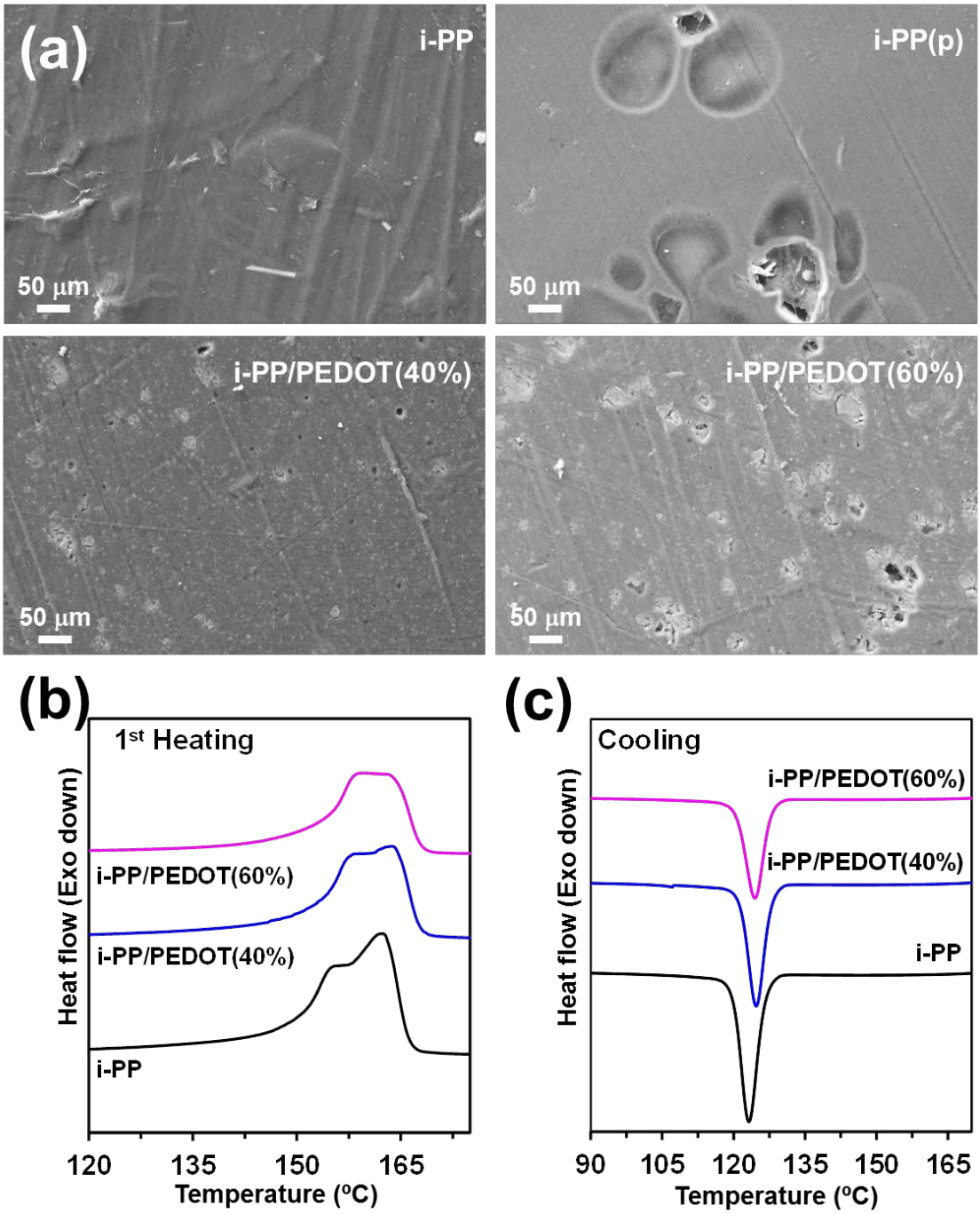
(a)
i-PP
50 μm
i-PP(p)
50 μm
i-PP/PEDOT(40%)
50 μm
i-PP/PEDOT(60%)
50 μm
(b)
1st Heating
Heat flow (Exo down)
i-PP/PEDOT(60%)
i-PP/PEDOT(40%)
i-PP
120
135
150
165
Temperature (ºC)
(c)
Cooling
Heat flow (Exo down)
i-PP/PEDOT(60%)
i-PP/PEDOT(40%)
i-PP
90
105
120
135
150
165
Temperature (ºC)

Figure 2

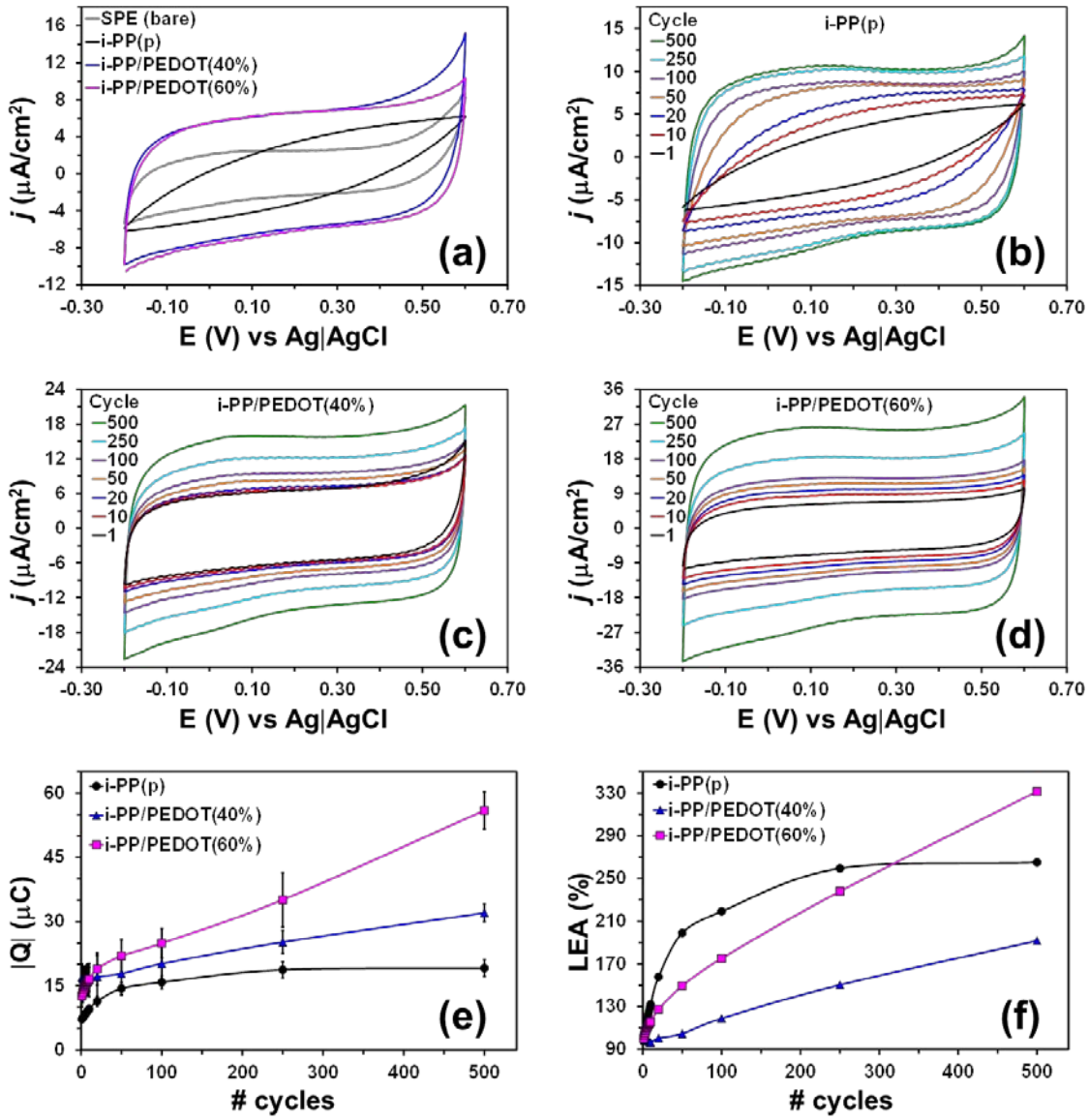
SPE (bare)
i-PP(p)
i-PP/PEDOT(40%)
i-PP/PEDOT(60%)
(a)
j (μA/cm²)
E (V) vs Ag|AgCl
Cycle
500
250
100
50
20
10
1
(b)
(c)
(d)
|Q| (μC)
cycles
(e)
LEA (%)
(f)

Figure 3

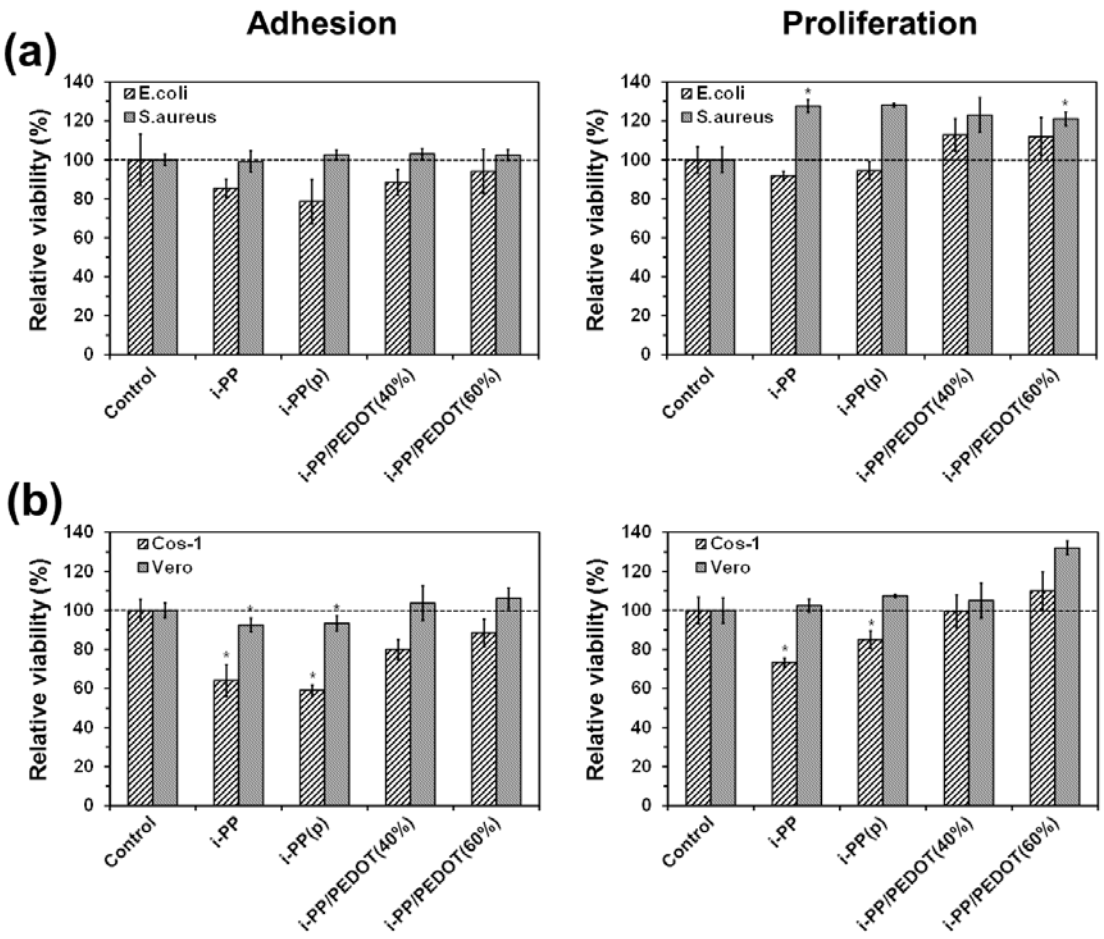
(a)
Adhesion
Proliferation
E.coli
S.aureus
Relative viability (%)
0
20
40
60
80
100
120
140
Control
i-PP
i-PP(p)
i-PP/PEDOT(40%)
i-PP/PEDOT(60%)
(b)
Cos-1
Vero

Figure 4

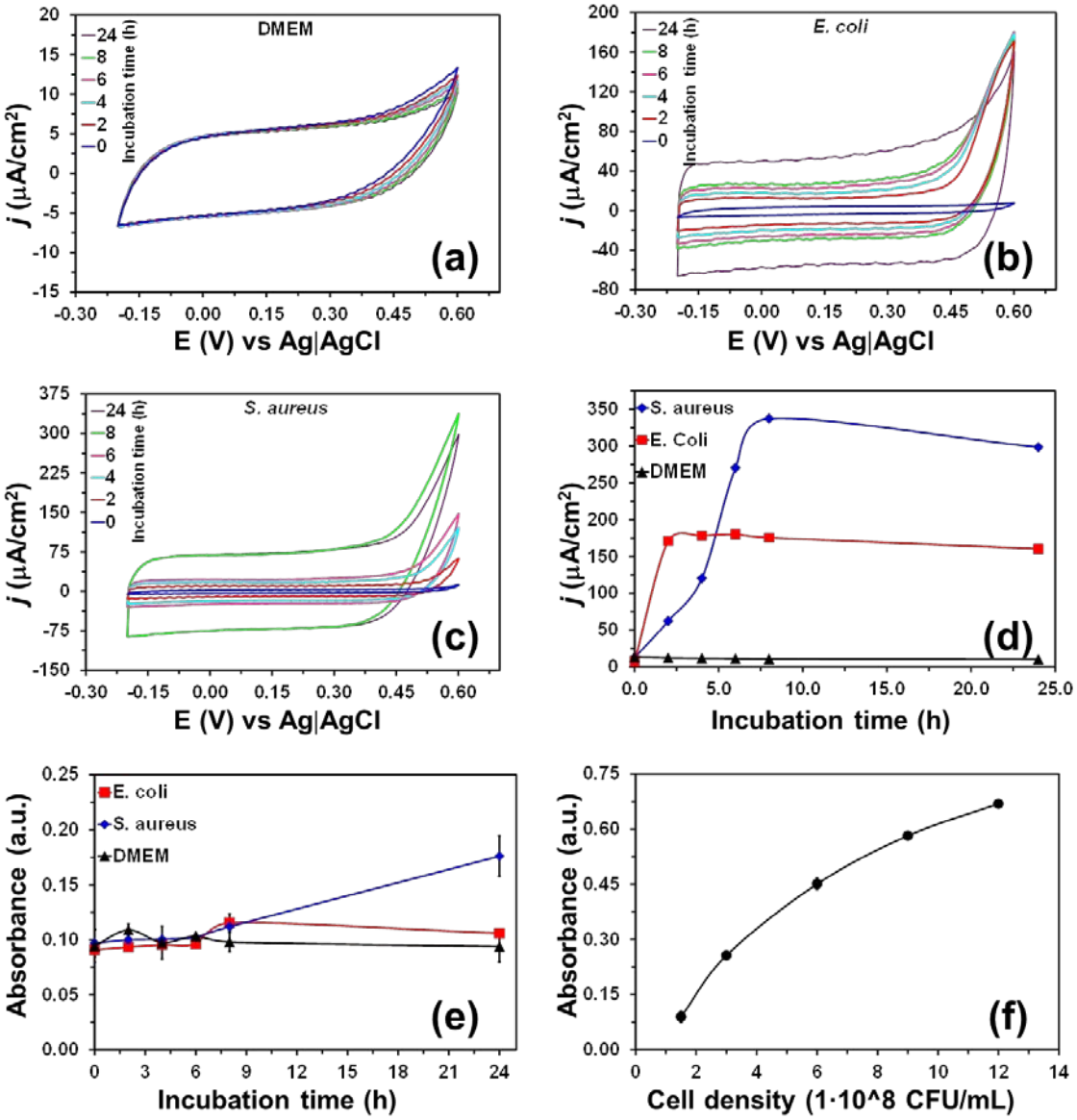
DMEM
Incubation time (h)
24
8
6
4
2
0
(a)
j (μA/cm²)
E (V) vs Ag|AgCl
E. coli
(b)
S. aureus
(c)
S. aureus
E. Coli
DMEM
(d)
Incubation time (h)
E. coli
S. aureus
DMEM
(e)
Absorbance (a.u.)
Incubation time (h)
(f)
Cell density (1·10^8 CFU/mL)

Figure 5

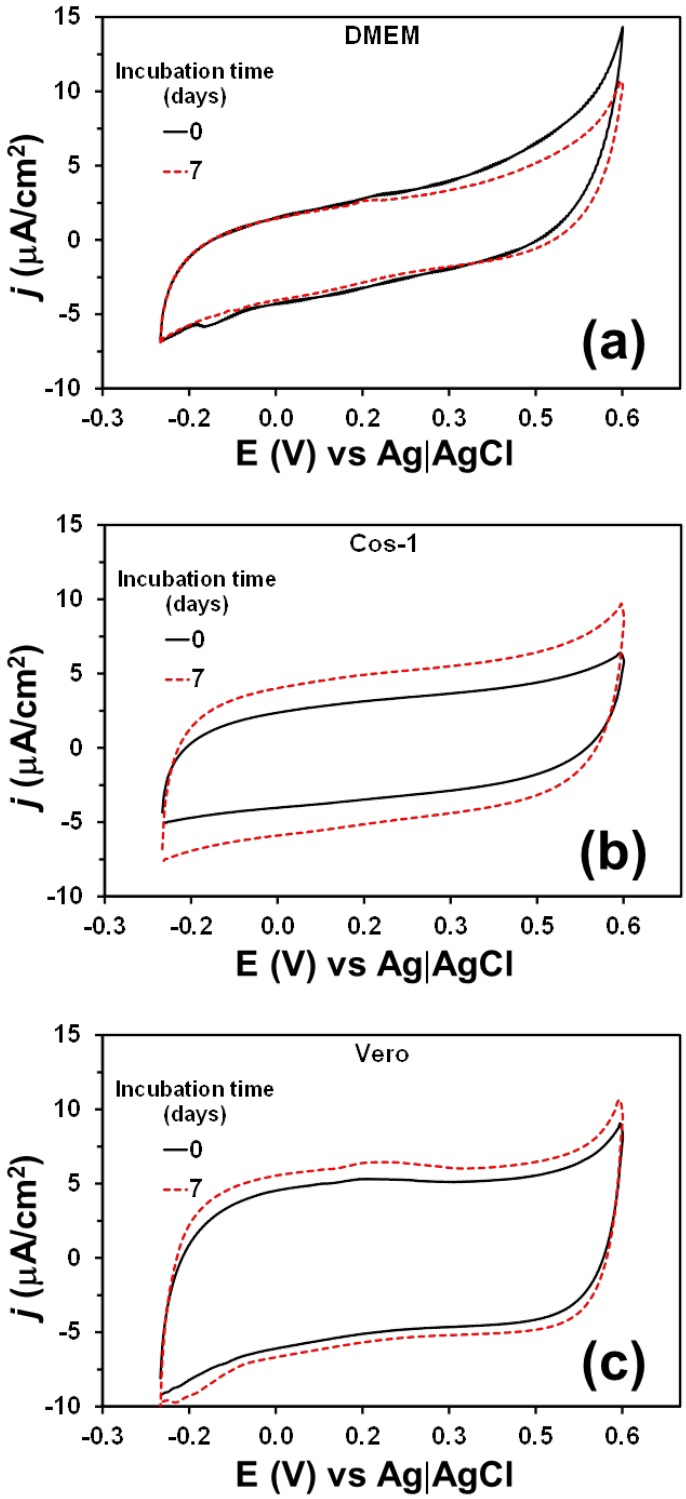
DMEM
Incubation time
(days)
—0
--7
(a)
j (μA/cm²)
E (V) vs Ag|AgCl
Cos-1
Incubation time
(days)
—0
--7
(b)
j (μA/cm²)
E (V) vs Ag|AgCl
Vero
Incubation time
(days)
—0
--7
(c)
j (μA/cm²)
E (V) vs Ag|AgCl

Figure 6

TOC Graphic

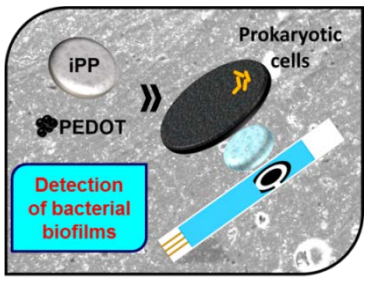
iPP
PEDOT
Prokaryotic cells
Detection of bacterial biofilms